J Mater Sci: Mater Electron (2021) 32:15907–15916

Electrical properties of Sr-modified CuO ceramics

Chang You[1], Zhicheng Li[1], Shuyan Zhang[1], Guoxiang Jiang[1], and Hong Zhang[1,*]

[1] School of Materials Science and Engineering, Central South University, Changsha 410083, China

Received: 12 March 2021
Accepted: 5 May 2021
Published online: 24 May 2021

ABSTRACT

CuO-based materials have broad scope of practical applications. Improving its conductivity might be important for enhancing the performance of CuO-based materials. Here, $Cu_{1-x}Sr_xO$ ceramics with various concentration of isovalent Sr-ion were prepared via a traditional solid reaction method. X-ray diffraction revealed that $Sr_{14}Cu_{24}O_{41}$ phase formed when Sr-ion was doped. $Sr_{14}Cu_{24}O_{41}$ phase has an incommensurately modulated structure with high conductivity. The quantity of $Sr_{14}Cu_{24}O_{41}$ phase increases with Sr-ion content and its distribution is almost homogenous in $Cu_{1-x}Sr_xO$ ceramics. The room-temperature resistivity ρ_{25} of $Cu_{1-x}Sr_xO$ ceramics shows significantly decrease even if with a very small amount of Sr-ion, such as the ρ_{25} of CuO is 114.18 kΩ cm and the one of $Cu_{0.99}Sr_{0.01}O$ ceramic is 32.69 Ω cm. The co-existing of Cu^{2+}, Cu^{+} ions, and existence of high conductive $Sr_{14}Cu_{24}O_{41}$ phase in the $Cu_{1-x}Sr_xO$ ceramics are responsible for their high conductivities.

1 Introduction

Among various oxides, CuO-based materials have been intensively studied for their broad scope of possible applications. For its narrow band gap (about 1.7 eV), CuO-based materials have been reported as efficient catalysis and photocatalyst materials [1–4], antibacterial agent [4], solar cells [5], semiconductor gas sensors [6, 7], and varistor [8] etc. For the low sintering temperature (~ 1000 °C), CuO-based materials could also be a potential candidate for application in low-temperature co-fired ceramics (LTCC). In the meantime, CuO-based materials were also studied as Li-ion electrode for the applications in Li-ion battery (LIB). As reported by Chen et al. [9], nanostructured CuO thin film showed high capacity, good cycling stability, excellent rate performance, and exhibited discharge capacities of 703 mA h·g^{-1} at 100 mA·g^{-1} and 465 mA h·g^{-1} at 1000 mA·g^{-1} even after 100 electrochemical cycles. Yang et al. [10] and Wang et al. [11] also reported that CuO-based ceramics showed adjustable temperature sensitivity by altering the content of each additive.

Improving of conductivity might be important for enhancing the performance of CuO-based materials. For example, Tilley et al. have reported a stable CuO-based photocathode for photoelectrochemical (PEC) H_2 generation, but the charge separation and transfer in CuO was low due to the low conductivity and carrier mobility, resulting in quite low photocurrent density [12, 13]. Defect engineering is widely applied in modifying the properties of semiconductors, by

Address correspondence to E-mail: hzhang@csu.edu.cn

https://doi.org/10.1007/s10854-021-06142-8

treating in various atmosphere conditions, doping with heterovalent ions and composite technology, etc. Wang et al. reported that the concentration of Cu vacancies in CuO can be tuned by changing the O_2 partial pressure during CuO thin-film treatment, and effectively improved the photoelectrochemical performance [3]. Like traditional semiconductors, the conductivity of CuO can also be tuned by doping with heterovalent ions, *e.g.*, the room-temperature resistivities (ρ_{25}) of CuO-based ceramics were reported to be effectively reduced by doping with Y^{3+}, Al^{3+}, or F^- [10, 11, 14]. For the enhanced conductivity with Cu_3N phase, the modified CuO thin-film electrode for LIB showed excellent electrochemical performance [15].

On the other hand, Tanaka et al. reported that CuO ceramics modified with small amounts of alkaline earth elements (MgO, CaO, SrO, or BaO) showed almost stable resistance at the applied electric fields from 0 to 500 kV/m [16, 17]. These indicate that the CuO-based ceramics doped with alkaline earth elements have potential applications in electronic components. In this work, CuO ceramics doped with various contents of Sr^{2+} ions were prepared. The influence of Sr^{2+} on the phase component and electrical properties were investigated in detail.

2 Experimental

CuO-based ceramics doped with isovalence Sr^{2+} ion were synthesized via traditional solid reaction method. Copper oxide (CuO, AR, Xilong Scientific Co., Ltd., China) and strontium carbonate ($SrCO_3$, AR, Xilong Scientific Co., Ltd., China) were utilized as the starting materials. Certain amount of CuO and $SrCO_3$ were weighed according to the nominal formula of $Cu_{1-x}Sr_xO$ (x = 0.001, 0.006, 0.01, 0.02, 0.05, 0.08, 0.10). Polyvinyl alcohol (PVA) solution was prepared by dissolving 8 g PVA into 100 mL deionized water. The raw materials were ground thoroughly in a mortar and proper amount of PVA solution was added as binder. Then, the mixture was pressed into block and calcined in muffle furnace at 700 °C for 1 h in air. The calcined block was ground again and granulated with appropriate content of PVA solution. The granulated powders were pressed into square slices with size of 28 × 12 × 2.5 mm^3, and then were further cut into rectangular bars with size of about 12 × 3 × 2.5 mm^3. These green bars were sintered at 980 °C–1000 °C for 1 h. After the as-sintered ceramics were polished and cleaned by ethanol, silver paste was painted at two ends of sample followed by being heated to 600 °C for 5 min to obtain the ohmic electrodes. CuO ceramics without Sr-dopant were also prepared as reference following the similar route described above, while the sintering temperature was 1060 °C.

Phase detection was conducted using X-Ray Diffraction (XRD, Rigaku D/max 2500, Japan) with Cu K_α radiation and λ of 0.154056 nm, with the diffraction angles (2θ) between 20° and 80° at scanning rate of 8° min^{-1}. Scanning electron microscopy (SEM, JEM 7900F) was employed to observe microstructure of the as-sintered ceramics, and element distribution in ceramics were investigated using energy-dispersive X-ray spectroscopy (EDS, Oxford Ultimax 65) in the SEM. Samples for SEM observation were either cross-sectional fracture areas or prepared by grinding, polishing, and Ar^+ ion milling. Temperature dependence of resistance (R-T) of each ceramic was tested using a resistance–temperature measurement system (ZWX-C, China) in direct current (DC) condition. The measurement temperature range was selected from room temperature up to 250 °C.

Relative density D_r of each sample was tested using Archimedes method according to Eq. (1):

$$D_r = \frac{\rho_W \cdot m_1/(m_1-m_2)}{\rho_0 \cdot \left(M_0/\sum_i n_i M_i\right)}, \quad (1)$$

where, ρ_W represents the density of deionized water, ρ_0 represents the theoretically density of CuO (6.5348 g cm^{-3}), M_0 is the molecular mass of CuO (79.545 g mol^{-1}), n_i and M_i represent the mole ratio and the relative atomic mass of each element respectively, m_1 is the sample weight in air. and m_2 is the weight in deionized water. Samples were polished and ultrasonically cleaned for 30 min followed by being dried in furnace thoroughly.

3 Results and discussion

3.1 Phase and microstructure

The XRD patterns of the as-sintered ceramics $Cu_{1-x}Sr_xO$ (x = 0, 0.02, 0.05, 0.1) are shown in Fig. 1a. Analyzed by MDI Jade 6, the main phase in all

samples can be confirmed to be the monoclinic CuO phase (ref. PDF 48-1548, space group of $C2/c$ (15)). In the samples for $x = 0.05$ and 0.1, some additional diffraction peaks belonging to a second phase can be detected. The second phase was identified to be $Sr_{14}Cu_{24}O_{41}$ phase with orthorhombic structure (ref. PDF 48-1496). These indicate the $Cu_{1-x}Sr_xO$ ceramics to be a CuO–$Sr_{14}Cu_{24}O_{41}$ composite system. Tanaka et al. also pointed out that there might be Sr–Cu–O complex oxide compounds in CuO ceramics containing small amounts of alkaline earth elements [17], but they failed to determine the detailed crystal structure. Figure 1b shows the magnified partial patterns in 2θ range of 34° and 41° the peaks in which correspond to $(11\bar{1})$ and (111) respectively. It can be seen that the diffraction peaks 2θ shift slightly to lower angle with increase of Sr-content, indicating the increasing of the lattice parameters. These also reveal that some Sr^{2+} ions have substituted into the CuO lattice. The substitution of Sr-ion leads to lattice expansion, because Sr^{2+} ion has larger ionic radius (0.118 nm) than that of Cu^{2+} ion (0.073 nm). There should be a limited solid solubility of Sr^{2+} ions in CuO lattice for the large difference of radii between Sr^{2+} and Cu^{2+} ions.

By refining the XRD patterns, the detailed lattice parameters of CuO phase in the studied ceramics are calculated and listed in Table 1. Lattice parameters (a, b, c and lattice volume) of as-prepared CuO without Sr-dopant are smaller than those of CuO crystal cited from PDF 48-1548. This could be ascribed to the occurrence of oxygen vacancies for insufficient ambient oxygen during the sintering process. Compared with the CuO without Sr-dopant, the lattice parameters of Sr-doped samples slightly increased with increase of Sr-content.

The $Sr_{14}Cu_{24}O_{41}$ crystal was initially synthesized and reported by Mc Carron et al. [18] and Siegrist et al. [19], both in 1988, though it was known as an impurity phase in Bi2212 superconductor single crystals [20]. $Sr_{14}Cu_{24}O_{41}$ has an incommensurately modulated structure [21–25]. The 3D framework of $Sr_{14}Cu_{24}O_{41}$ crystal lattice is illustrated in Fig. 2a, which is consulted from the report by Gotoh et al. [26]. In the $Sr_{14}Cu_{24}O_{41}$ crystal lattice, each of the repeat unit is composed of two Sr^{2+} layers, a quasi-one-dimensional [Cu_2O_3] spin ladder layer (shown in Fig. 2b) and an edge-shared [CuO_2] spin chain layer (shown in Fig. 2c). Each Sr^{2+} layer locates between ladder layer and chain layer (see in Fig. 2d and e). These layers alternately stack along b direction following the sequence of ladder-Sr-chain-Sr-ladder while extending along c direction. The ratio of the length of ($Sr_2Cu_2O_3$) ladder unit and (CuO_2) chain unit along c direction was reported to be approximately 0.7, leading to the chemical formula of $(Sr_2Cu_2O_3)_{0.7}(CuO_2)$, converted into $Sr_{14}Cu_{24}O_{41}$ [27].

Figure 3 shows SEM observations of $Cu_{1-x}Sr_xO$ ceramics ($x = 0$, 0.02, 0.05, 0.1). The average grain size of pure CuO ceramic is approximately 10 μm (see in Fig. 3a). The one for $x = 0.02$ ceramic is similar to that of the pure CuO sample, but small particles emerges at the grain boundaries which might be the second phase. The average sizes of grains are about 6 μm and

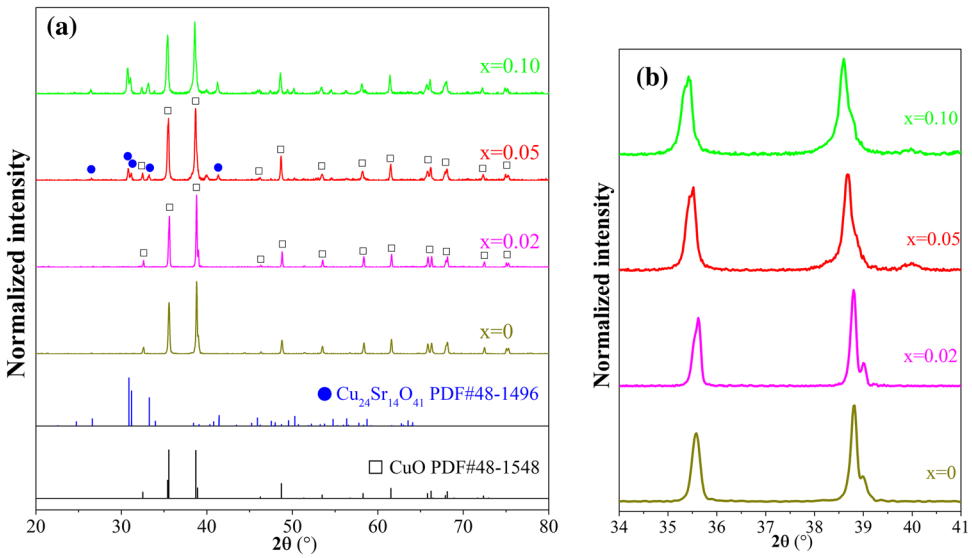

Fig. 1 XRD patterns of the as-sintered ceramics $Cu_{1-x}Sr_xO$ ($x = 0$, 0.02, 0.05, 0.1): **a** overall patterns; **b** partial magnified areas

Table 1 Lattice parameters of CuO phase in $Cu_{1-x}Sr_xO$ (x = 0, 0.02, 0.05, 0.10) ceramics refined from the XRD patterns as shown in Fig. 1

Sr-content x	a (nm)	b (nm)	c (nm)	β (°)	*Lattice volume* (nm^3)
PDF 48-1548	0.4688	0.3423	0.5132	99.51	0.0812
0	0.4679	0.3418	0.5128	99.56	0.0809
0.02	0.4683	0.3418	0.5127	99.52	0.0810
0.05	0.4688	0.3422	0.5131	99.50	0.0812
0.10	0.4696	0.3426	0.5138	99.44	0.0816

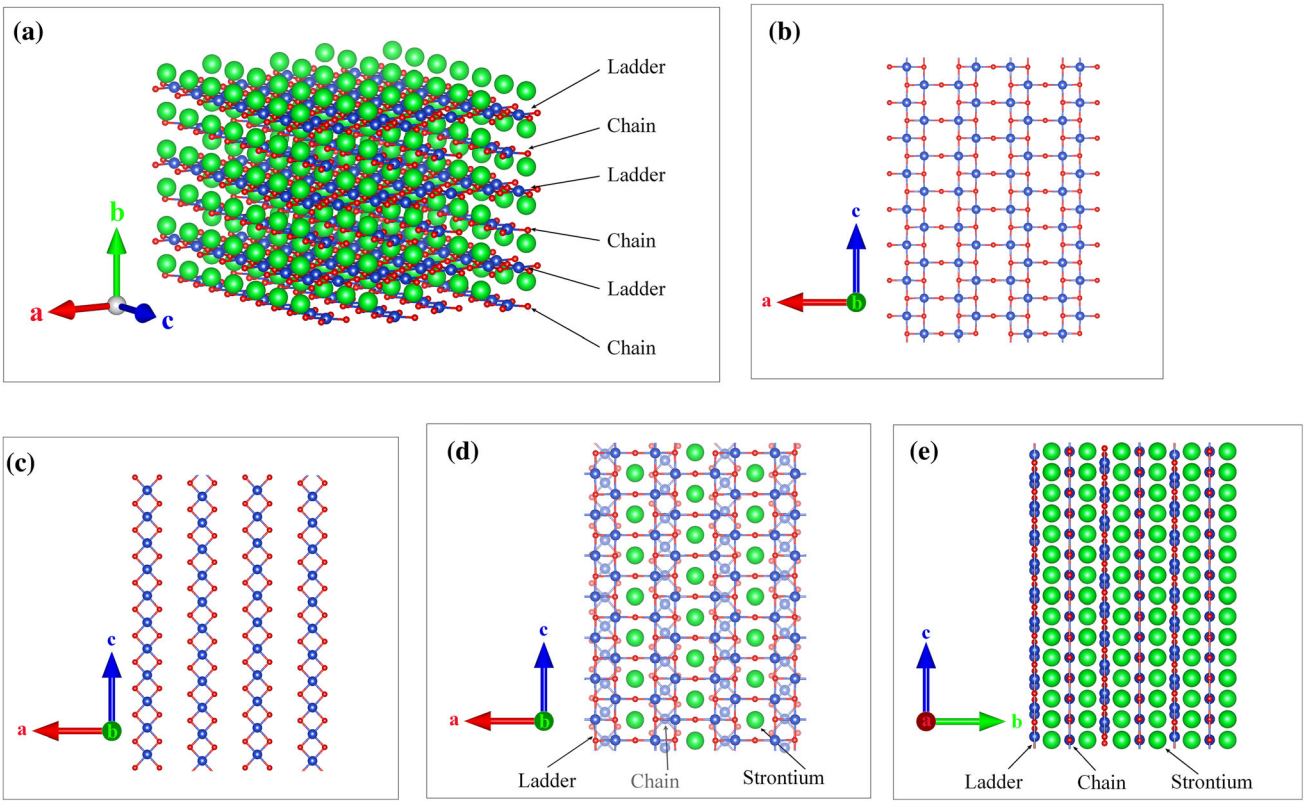

Fig. 2 Structural schematics of adaptive misfit compound $Sr_{14}Cu_{24}O_{41}$, **a** 3d architecture of overall component, **b** [Cu_2O_3] ladder layer, **c** [CuO_2] chain layer, **d** stacking structure view along b orientation, and **e** stacking structure view along a orientation

8μm for the ceramics with x = 0.05 and 0.1, respectively. All the samples contain some pores. Tested by using Archimedes method and calculated with Eq. (1), the relative densities of the $Cu_{1-x}Sr_xO$ ceramics were 92.85%, 94.20%, 94.10%, 91.59%, 88.74% and 87.20% for x is 0, 0.01, 0.02, 0.05, 0.08 and 0.1 respectively.

To further investigate the distribution of elements in the studied composite ceramics, EDS analysis was carried out. Figure 4 shows the analysis results of cross section of pure CuO and $Cu_{0.98}Sr_{0.02}O$ ceramics. Figure 4a–c shows the SEM secondary electron image and the related element distribution mappings corresponding to Cu, O in CuO ceramic, respectively. Figure 4d–g shows the SEM secondary electron image and the element distribution mappings corresponding to Cu, O, and Sr of $Cu_{0.98}Sr_{0.02}O$ ceramic, respectively. Apparently, compared with undoped CuO, element Sr accumulated at the small particles in $Cu_{0.98}Sr_{0.02}O$ ceramic, confirming those small particles to be Sr-rich second phase, which is named as $Sr_{14}Cu_{24}O_{41}$ according to the XRD results shown in Fig. 1.

Figure 5 shows the microstructural and element distribution analysis of a $Cu_{0.95}Sr_{0.05}O$ ceramic which was Ar^+ polished. Figure 5a is a SEM secondary electronic image, and Fig. 5b–d shows the element distribution mappings corresponding to Cu, O, and Sr, respectively. Similar to the results from cross-sectional observation of $Cu_{0.98}Sr_{0.02}O$ ceramic

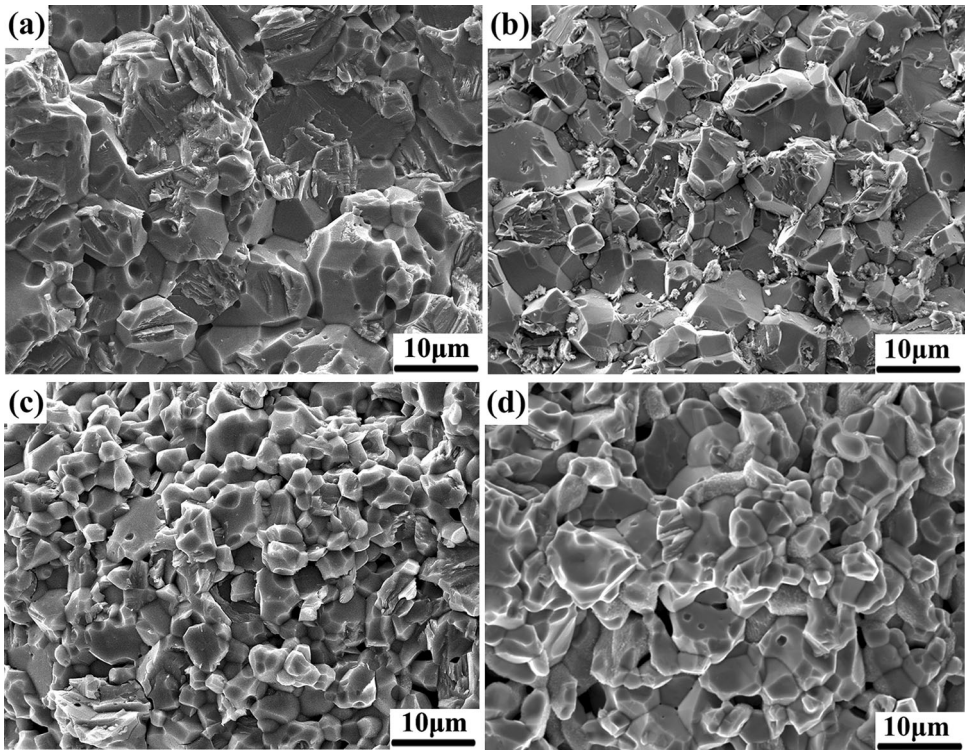

Fig. 3 SEM images of cross-sectional fracture surface in $Cu_{1-x}Sr_xO$ ceramics with various contents of Sr-dopants, **a** $x = 0$, **b** $x = 0.02$, **c** $x = 0.05$, and **d** $x = 0.10$

described in Fig. 4, Cu and O elements distribute almost uniformly, while Sr mainly locates at some areas where second phase is locating. Furthermore, the ceramic with higher Sr-content ceramic, $Cu_{0.9}Sr_{0.1}O$, was also investigated, as shown in Fig. 6. Figure 6a shows the analysis of the cross-sectional observation of $Cu_{0.9}Sr_{0.1}O$ ceramic in lower magnification. Figure 6b–d shows the element distribution mappings corresponding to Cu, O, and Sr, respectively. Compared with the results shown in Figs. 4 and 5, the quantity of Sr-rich regions increased and almost homogeneously distributed in the $Cu_{0.9}Sr_{0.1}O$ ceramic.

3.2 Ionic valence state

To analyze the valence state of ions, XPS investigations were carried out on CuO, $Cu_{0.99}Sr_{0.01}O$, and $Cu_{0.95}Sr_{0.05}O$ ceramics, and the results are fitted with Thermo Avantage soft. Figure 7a shows the XPS full patterns for the ceramics. The peaks for Sr element can be detected even in both two doped samples. The Cu $2p_{3/2}$ narrow spectra are shown in Fig. 7b. Each spectrum is composed of a $2p_{3/2}$ peak and a satellite peak. The fitted results reveal that each of $2p_{3/2}$ peaks is distinguished into two peaks ascribed to Cu^+ and Cu^{2+} ions, respectively, while the satellite peaks are composed of three peaks which are in agreement with the report by Biesinger et al. [28]. The fitted binding energies of Cu^+ and Cu^{2+} ions are shown in Table 2.

The concentration ratio of Cu^{2+} ions comparing to all Cu-ions in each ceramic can be calculated by Eq. (2) [28]:

$$r_{Cu^{2+}} = \frac{B + A_1}{A + B} \times 100\%, \quad (2)$$

where A represents whole area covered by the Cu $2p_{3/2}$ peak, A_1 is the area for the fitted peak of Cu^{2+} ions, and B represents the area of the satellite peak. As reported by Ghijsen et al. [29], Cu^+ ion makes no contribution to the Cu 2p satellite peak. The different XPS characteristic between Cu^{2+} and Cu^+ ions mainly results from the different 3d electronic configuration, i.e., Cu^{2+} ion has open-shell $3d^9$, while Cu^+ ion contains closed-shell $3d^{10}$ electronic configuration. This indicates that all the satellite peaks come from Cu^{2+} ions. The calculated ratios are shown in Table 2. The co-existing of Cu^{2+} and Cu^+ ions in the ceramics is consistent with the discussion in Fig. 1 that the formation of oxygen vacancies in the CuO lattice. These also indicate that the CuO phase in the studied $Cu_{1-x}Sr_xO$ ceramics ought to be nonstoichiometric compound. The concentration of Cu^{2+}

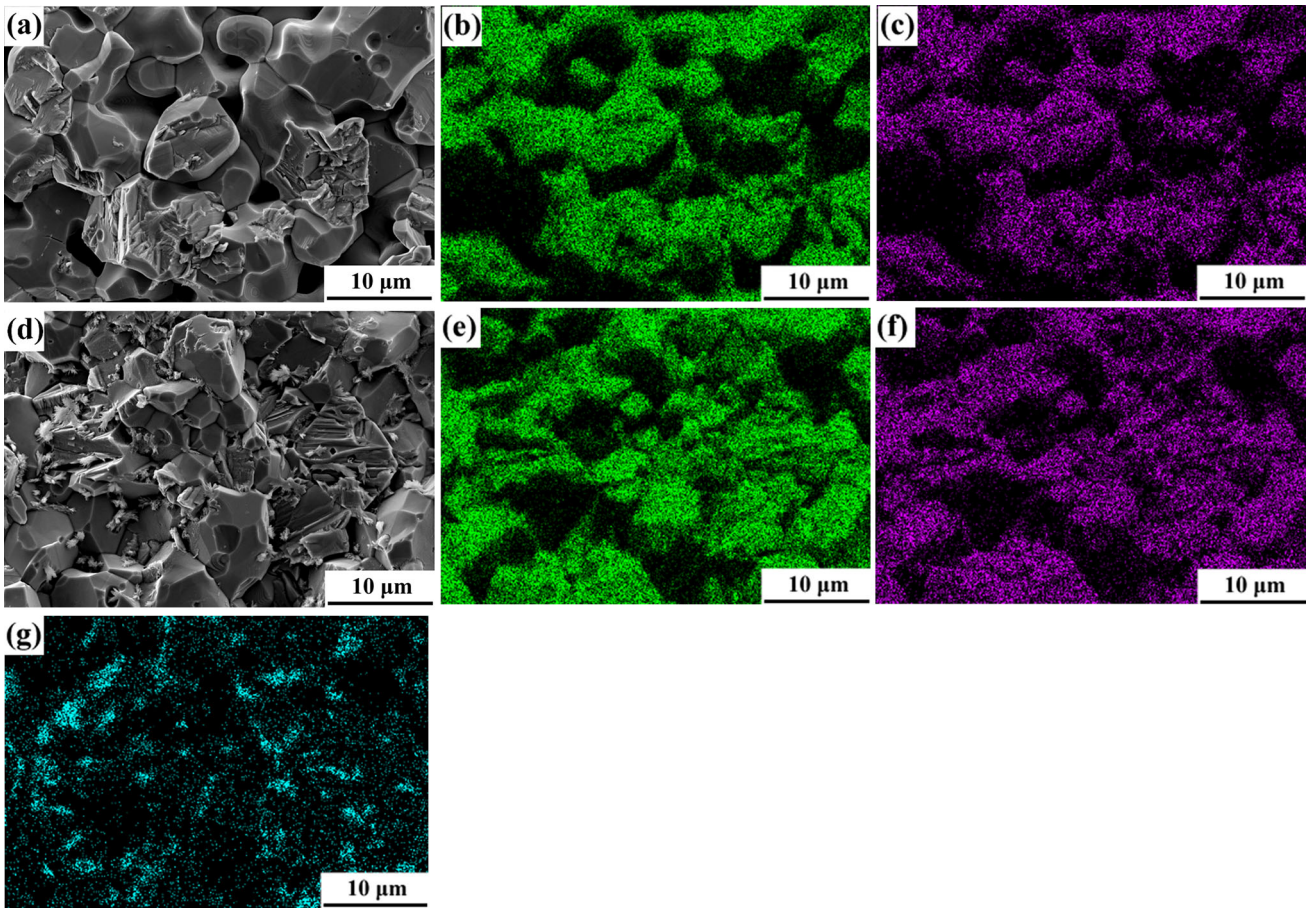

Fig. 4 EDS analysis of element distribution in CuO and $Cu_{0.98}Sr_{0.02}O$ ceramic: **a** SEM image of CuO ceramic, **b** Cu mapping of CuO ceramic, **c** O mapping of CuO ceramic, **d** SEM image of $Cu_{0.98}Sr_{0.02}O$ ceramic, **e** Cu mapping of $Cu_{0.98}Sr_{0.02}O$ ceramic, **f** O mapping of $Cu_{0.98}Sr_{0.02}O$ ceramic, and **g** Sr mapping of $Cu_{0.98}Sr_{0.02}$ of $Cu_{0.98}Sr_{0.02}O$ ceramic

ions increased with increase of the Sr-content. Figure 7c shows O 1 s narrow patterns of CuO and $Cu_{0.99}Sr_{0.01}O$ ceramic. The peaks located at 529.5 eV and 531.2 eV are identified as lattice oxygen and adsorbed oxygen, respectively [30, 31].

3.3 Electrical properties

Figure 8a presents the plot of room-temperature resistivity (ρ_{25}) as function of Sr-content in the $Cu_{1-x}Sr_xO$ ceramics. The ρ_{25} of $Cu_{1-x}Sr_xO$ (x = 0, 0.001, 0.006, 0.01, 0.02, 0.05, 0.08, 0.10) ceramics is 114.18 kΩ·cm, 91.69, 71.39, 32.69, 13.96, 4.74, 3.44, and 2.70 Ω·cm, respectively. It is interesting that, compared to the pure CuO, the ρ_{25} of the Sr-doped CuO ceramics shows a significantly decrease (even if a very small amount of Sr-ion was introduced). This indicates that the addition of Sr-ion plays a key role in the conductivity improvement of CuO ceramic, although Sr^{2+} and Cu^{2+} ions have the same valence.

Figure 8b shows the plots of temperature dependence of resistivity in Arrhenius plot of $Cu_{1-x}Sr_xO$ ceramics (x = 0, 0.001, 0.006, 0.01, 0.02, 0.05, 0.08, and 0.10) with various contents of Sr-ions. All samples possess typical semiconducting characteristics for that the resistivity decreases with the increase of temperature.

CuO is a semiconductor oxide and has a band gap of about 1.7 eV. If a CuO crystal is an ideal crystal without any lattice defect, it is an electrical insulator. Due to the insufficient oxygen in the sintering environment, it is possible that oxygen vacancies formed during sintering. The related defect reaction can be described in the Kröger–Vink symbol, as shown in Eqs. (3) and (4):

$$O_O \xrightarrow{CuO} V_{\ddot{O}} + 2e' + \frac{1}{2}O_2 \quad (3)$$

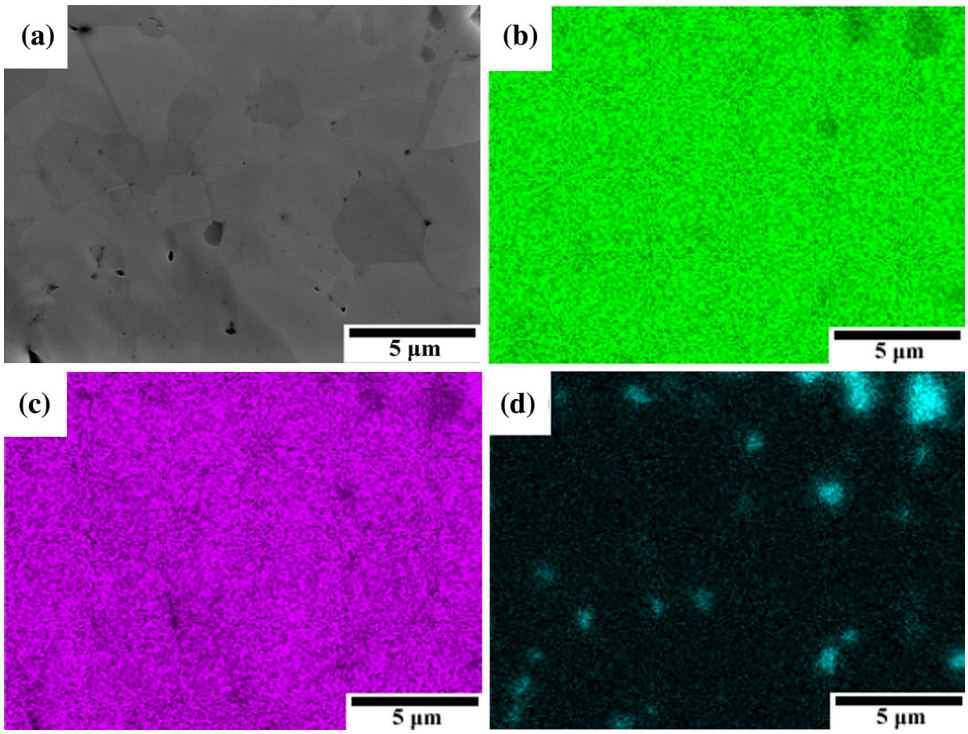

Fig. 5 EDS analysis of element distribution in $Cu_{0.95}Sr_{0.05}O$ ceramic: **a** SEM image; **b** Cu mapping; **c** O mapping; **d** Sr mapping

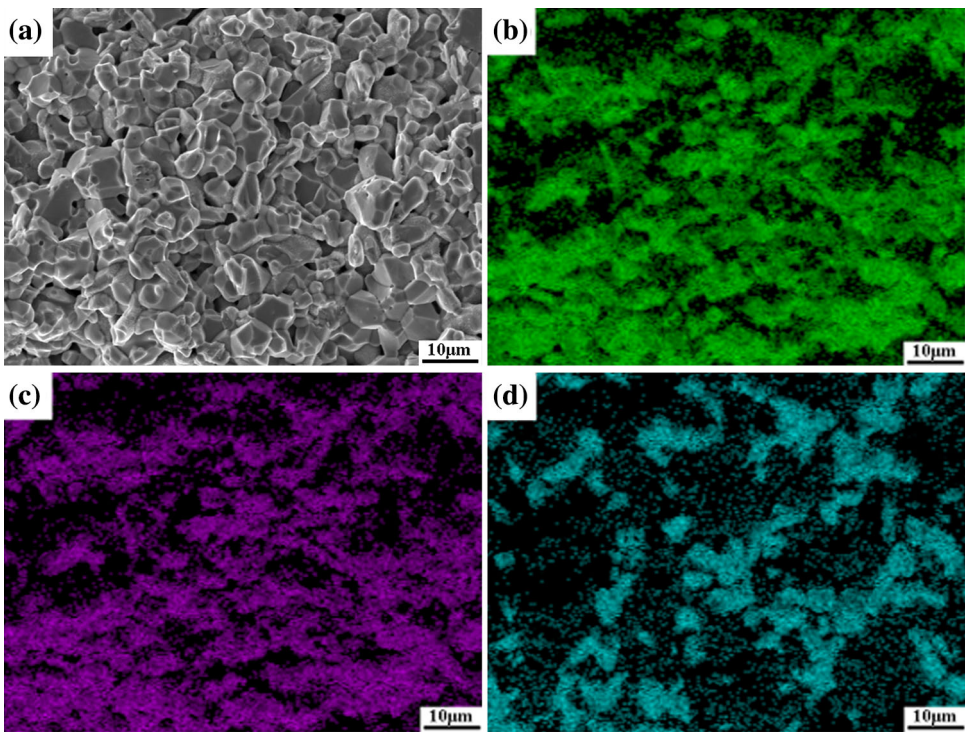

Fig. 6 EDS detection of element distribution in $Cu_{0.9}Sr_{0.1}O$ ceramic: **a** SEM image; **b** Cu mapping; **c** O mapping; **d** Sr mapping

$$e' + Cu_{Cu} \xrightarrow{CuO} Cu'_{Cu}. \quad (4)$$

Oxygen escapes from the lattice for insufficient oxygen environment and electrons left in the lattice, as shown in Eq. (3). The electrons act as weakly bound electrons and locate at the donor level, which can be thermally activated and jump to the conduction band. On the other hand, some of the electrons might also be captured by Cu-cations, and then, Cu^{2+}

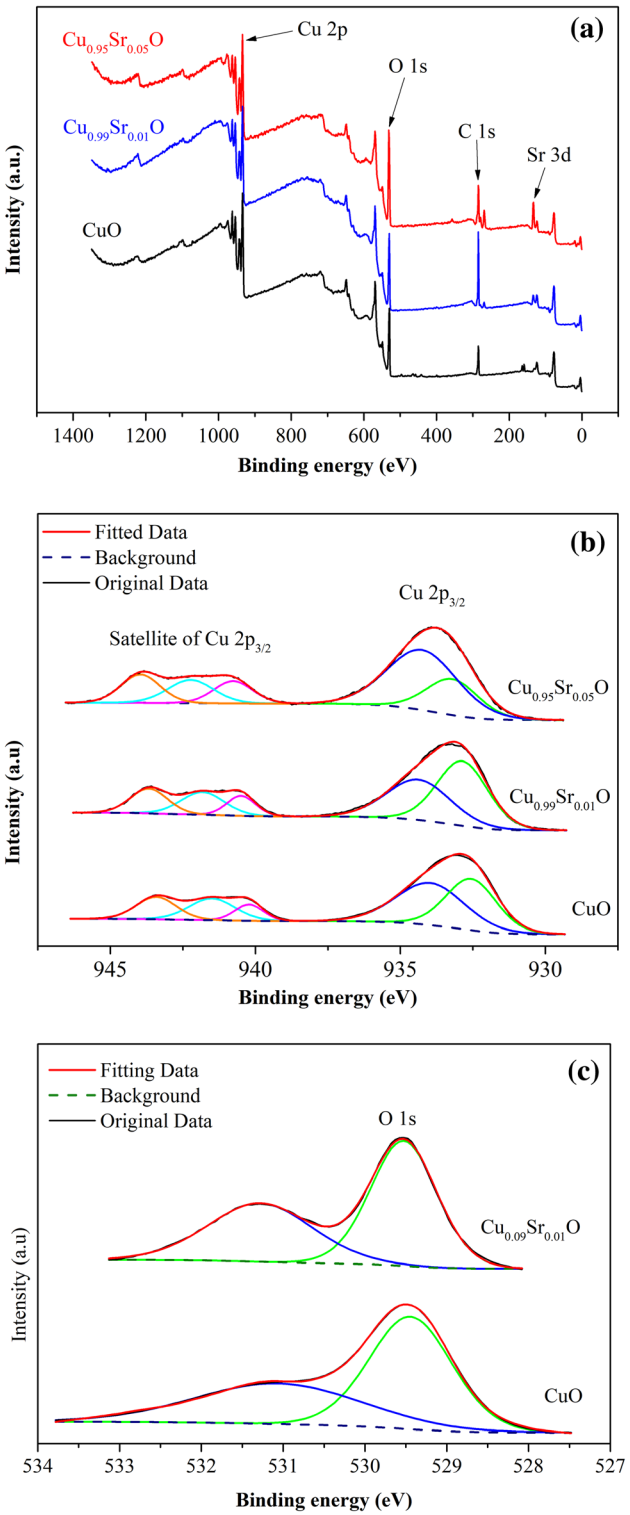

Fig. 7 XPS analysis of the CuO, $Cu_{0.99}Sr_{0.01}O$ and $Cu_{0.95}Sr_{0.05}O$ ceramics: **a** full patterns, **b** Cu $2p_{3/2}$ patterns, and **c** O 1 s patterns

changed to Cu^{+} ion, as shown in Eq. (4). Therefore, the prepared CuO ceramic should be a nonstoichiometric compound and its conductivity increases.

It is well known that the conductivity of a semiconductor can be adjusted by doping with various contents of heterovalent elements such as donors or acceptors. Sr- and Cu-ions are isovalent cations, and therefore, Sr-ion could act as neither donor nor acceptor for CuO-based semiconductor. However, as shown in Fig. 8, ρ_{25} of $Cu_{1-x}Sr_xO$ ceramics significantly reduced even if a small content of Sr-ion was added, and the ρ_{25} decreased monotonously with the increase of Sr-ion content. These indicate that the influence of Sr-ion in the electrical properties of $Cu_{1-x}Sr_xO$ ceramics must originate from some factors instead of semiconductor doping. According to the above discussion, $Sr_{14}Cu_{24}O_{41}$ phase formed when a small content of Sr-ions were added into CuO ceramics and the $Sr_{14}Cu_{24}O_{41}$ phase could play a key role in enhancing electrical conductivity of the ceramics.

Theoretically, it can be calculated that 6 holes form in a single unit of $Sr_{14}Cu_{24}O_{41}$ due to its intrinsic character of excess O anions. However, only a limited ratio of the holes is located in the ladder layer, especially where they can contribute to the outstanding conductivity of the $Sr_{14}Cu_{24}O_{41}$ phase. Those holes on the ladder layers are partly localized under low temperature due to the existence of an energy barrier called 'spin gap' and can only migrate along the *c* direction contributing to one-axis conductivity [22]. However, with the temperature increasing, the holes are thermally activated and can also transfer from ladder layer to chain layer [24–26]. The temperature dependence of electrical resistivity of $Sr_{14}Cu_{24}O_{41}$ is semiconductor characteristic and holes in the ladder are concluded to be dominant to the electrical conductivity [32, 33]. Therefore, one can get that $Sr_{14}Cu_{24}O_{41}$ phase has self-doping characteristics and shows high conductivity. The quantity of $Sr_{14}Cu_{24}O_{41}$ phase increases with increase Sr-ion content, and distribution of $Sr_{14}Cu_{24}O_{41}$ phase is almost homogenous in $Cu_{1-x}Sr_xO$ ceramics.

4 Conclusion

CuO-based ceramics modified with Sr^{2+} ions ($Cu_{1-x}Sr_xO$, *x* ranges from 0 to 0.1) were obtained via traditional solid reaction method. The prepared CuO-based ceramics containing Sr^{2+} additives are composed of monoclinic CuO phase and incommensurately modulated $Sr_{14}Cu_{24}O_{41}$ phase. The quantity of

Table 2 Fitted results of Cu $2p_{3/2}$ spectra in CuO, $Cu_{0.99}Sr_{0.01}O$ and $Cu_{0.95}Sr_{0.05}O$ ceramics

	Binding energy of Cu^{+} (eV)	Binding energy of Cu^{2+} (eV)	Concentration Cu^{2+} (%)
CuO	932.56	933.97	66.95
$Cu_{0.99}Sr_{0.01}O$	932.87	934.38	66.97
$Cu_{0.95}Sr_{0.05}O$	933.21	934.25	79.50

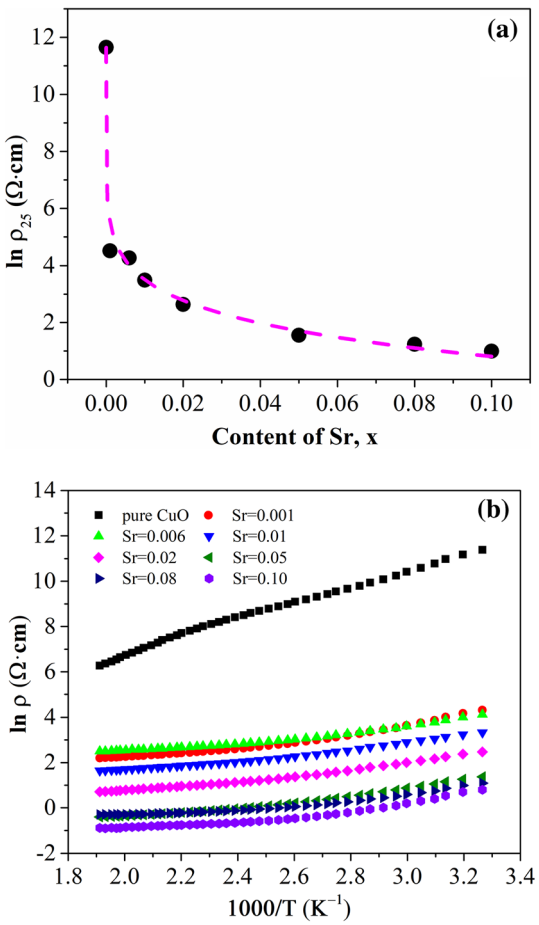

Fig. 8 Electrical properties of $Cu_{1-x}Sr_xO$ ceramics (x = 0, 0.001, 0.006, 0.01, 0.02, 0.05, 0.08, 0.10): **a** $\ln\rho_{25}$ dependence of Sr-content; **b** lnρ-1000/T plots for various Sr-contents

$Sr_{14}Cu_{24}O_{41}$ phase increases with Sr-ion content and its distribution is almost homogenous in $Cu_{1-x}Sr_xO$ ceramics. Room-temperature resistivity ρ_{25} of $Cu_{1-x}Sr_xO$ (x = 0, 0.001, 0.006, 0.01, 0.02, 0.05, 0.08, 0.10) ceramics is 114.18 kΩ cm, 91.69, 71.39, 32.69, 13.96, 4.74, 3.44, and 2.70 Ω cm, respectively. It shows significantly decrease even if with a very small amount Sr doping. The co-existing of Cu^{2+}, Cu^{+} ions, and existence of high conductive $Sr_{14}Cu_{24}O_{41}$ phase in the $Cu_{1-x}Sr_xO$ ceramics are responsible for their high conductivities.

Acknowledgements

This work is supported by the research funding from the Hunan Wedid Materials Technology Co., Ltd., China (Grant No. 738010241), the National Natural Science Foundation of China (Grant No. 51767021), and the Research and Development Program in Key Areas of Guangdong Province (Grant No. 2019B090913002).

References

1. M. Zhu, G. Diao, High catalytic activity of CuO nanorods for oxidation of cyclohexene to 2-cyclohexene-1-one. Catal. Sci. Tech. **2**, 82–84 (2012)
2. Y. Chen, Z. Shen, Q. Jia, J. Zhao, Z. Zhao, H. Ji, A CuO–ZnO nanostructured p–n junction sensor for enhanced N-butanol detection. RSC Adv. **6**, 2504–2511 (2016)
3. Z. Wang, L. Zhang, T.U. Schülli, Y. Bai, S.A. Monny, A. Du, L. Wang, Identifying copper vacancies and their role in the CuO based photocathode for water splitting. Angew. Chem. Int. Ed. **58**, 17604–17609 (2019)
4. K. Kumar, A. Priya, A. Arun, S. Hait, A. Chowdhury, Antibacterial and natural room-light driven photocatalytic activities of CuO nanorods. Mater. Chem. Phys. **226**, 106–112 (2019)
5. S. Anandan, X. Wen, S. Yang, Room temperature growth of CuO nanorod arrays on copper and their application as a cathode in dye-sensitized solar cells. Mater. Chem. Phys. **93**, 35–40 (2005)
6. D.R. Miller, S.A. Akbar, P.A. Morris, Nanoscale metal oxide-based heterojunctions for gas sensing: a review. Sens. Actuators B **204**, 250–272 (2014)
7. P. Horak, V. Bejsovec, J. Vacik, V. Lavrentiev, M. Vrnata, M. Kormunda, S. Danis, Thin copper oxide films prepared by ion beam sputtering with subsequent thermal oxidation: application in chemiresistors. Appl. Surf. Sci. **389**, 751–759 (2016)
8. T.D. Cheng, H. Zhang, N. Liu, P.F. Yu, G.T. Wu, X.G. Tang, Improvement of memristive properties in CuO films with a seed Cu layer. Appl. Phys. Lett. **114**, 061602 (2019)

9. W. Chen, H. Zhang, Z. Ma, B. Yang, Z. Li, High electrochemical performance and lithiation–delithiation phase evolution in CuO thin films for Li-ion storage. J. Mater. Chem. A. **3**, 14202–14209 (2015)
10. B. Yang, H. Zhang, J. Zhang, X. Zhang, Z. Li, Electrical properties and temperature sensitivity of B-substituted CuO-based ceramics for negative temperature coefficient thermistors. J. Mater. Sci. Mater. Electron. **26**, 10151–10158 (2015)
11. X. Wang, Z. Li, W. Yan, P. Wang, H. Zhang, Electrical properties of Nb/Al-doped CuO-based ceramics for NTC thermistors. Process. Appl. Ceram. **14**, 47–55 (2020)
12. W. Septina, R.R. Prabhakar, R. Wick, T. Moehl, S.D. Tilley, Stabilized solar hydrogen production with CuO/CdS petero-junction thin film photocathodes. Chem. Mater. **29**, 1735–1743 (2017)
13. P. Samarasekara, M.M. Arachchi, A. Abeydeera, C. Fernando, A. Disanayake, R. Rajapakse, Photocurrent enhancement of d.c. sputtered copper oxide thin films. Bull. Mater. Sci. **28**(5), 483–486 (2006)
14. H. Li, S. Gong, B. Yang, J. Zhang, H. Zhang, Electrical conductivity and temperature sensitivity of W/F-modified CuO-based ceramics. Nonferrous Metals Sci. Eng. **7**, 54–59 (2016)
15. W. Chen, H. Zhang, B. Yang, B. Li, Z. Li, Characterization of Cu_3N/CuO thin films derived from annealed Cu_3N for electrode application in Li-ion batteries. Thin Solid Films **672**, 157–164 (2019)
16. S. Tanaka, Y. Sawai, A. Chiba, K. Takahashi, Y. Saito, Ceramic resistors based on copper oxides. Key Eng. Mater. **228–229**, 229–232 (2002)
17. S. Tanaka, Y. Sawai, A. Chiba, Electrical properties and microstructure of CuO ceramics containing small amounts of alkaline earth elements. J. Eur. Ceram. Soc. **24**, 289–293 (2004)
18. E.M. Mc Carron, M.A. Subramanian, J.C. Calabrese, R.L. Harlow, The incommensurate structure of $(Sr_{14-x}Ca_x)Cu_{24}O_{41}$ ($0 < x \sim 8$) a superconductor byproduct. Mater. Res. Bull. **23**, 1355–1356 (1988)
19. T. Siegrist, L.F. Schneemeyer, S.A. Dunshine, J.V. Waszczak, R.S. Roth, A new layered cuprate structure-type, $(A_{1-x-}A'_x)_{14}Cu_{24}O_{41}$. Mater. Res. Bull. **23**, 1429–1438 (1988)
20. K.M. Kojima, N. Motoyama, H. Eisaki, S. Uchida, The electronic properties of cuprate ladder materials. J. Electron. Spectrosc. **117–118**, 237–250 (2001)
21. L. Cheng, L.L. Wang, S.Z. Pu, N. Hu, Y. Zhang, Y. Liu, W. Wei, R. Xiong, J. Shi, Structure and electric transport properties of the spin ladder compound $Sr_{14}(Cu_{0.97}M_{0.03})_{24}O_{41}$ (M=Zn,Ni,Co). Acta Phys. Sinica. **59**, 1155–1162 (2010)
22. G.C. Deng, D.H. Yu, R. Mole, E. Pomjakushina, K. Conder, M. Kenzelmann, S. Yano, C.W. Wang, K.C. Rule, J.S. Gardner, Spin dynamics of edge-sharing spin chains in $SrCa_{13}Cu_{24}O_{41}$. Phys. Rev. B. **98**, 184411 (2018)
23. Z. Hiroi, S. Amelinckx, G. Van Tendeloo, N. Kobayashi, Microscopic origin of dimerizatino in the CuO_2 in $Sr_{14}Cu_{24}O_{41}$. Phys. Rev. B. **54**, 15849–15855 (1996)
24. Y. Gotoh, I. Yamaguchi, Y. Takahashi, J. Akimoto, S. Mizuta, M. Onoda, H. Fujino, T. Nagata, J. Akimitsu, Modulated structure analysis of composite crystal $(Sr_2Cu_2O_3)_{0.70}CuO_2$, "$Sr_{14}Cu_{24}O_{41}$" with two-legged ladder and one-dimensional chain. Ferroelectrics **250**, 19–22 (2000)
25. G. Deng, N. Tsyrulin, P. Bourges, D. Lamago, H. Ronnow, M. Kenzelmann, S. Danilkin, E. Pomjakushina, K. Conder, Spin-gap evolution upon Ca doping in the spin-ladder series $Sr_{14-x}Ca_xCu_{24}O_{41}$ studied by inelastic neutron scattering. Phys. Rev. B. **88**, 014504 (2013)
26. Y. Gotoh, I. Yamaguchi, H. Eisaki, T. Nagata, J. Akimitsu, Temperature dependence of atomic modulation in the incommensurate composite crystal structure of $(Sr_2Cu_2O_3)_{0.70}CuO_2$, '$Sr_{14}Cu_{24}O_{41}$.' Phys. C **445**, 107 (2005)
27. G. Yoshito, Accurate determination of composite crystal structure of incommensurately modulated $Sr_{14}Cu_{24}O_{41}$ using the Akaike information criterion. J. Phys. Soc. Jap. **87**(12), 124601 (2018)
28. M.C. Biesinger, L.W.M. Lau, A.R. Gerson, R.S.C. Smart, Resolving surface chemical states in XPS analysis of first row transition metals, oxides and hydroxides: Sc, Ti, V. Cu and Zn. Appl. Surf. Sci. **257**(3), 887–898 (2010)
29. J. Ghijsen, L.H. Tjeng, J. van Elp, H. Eskes, J. Westerink, G.A. Sawatzky, Electronic structure of Cu_2O and CuO. Phys. Rev. B **38**(16), 11322–11330 (1988)
30. Y. Dong, X.Y. Jiang, J.H. Mo, Y.Z. Zhou, J.P. Zhou, Hollow CuO nanoparticles in carbon microsphere prepared from cellulose-cuprammonium solution as anode materials for Li-ion batteries. Chem. Eng. J. **381**, 122614 (2020)
31. Z.H. Ai, L.Z. Zhang, S.C. Lee, W.K. Ho, Interfacial hydrothermal synthesis of Cu@Cu_2O core-shell microspheres with enhanced visible-light-driven photocatalytic activity. J. Phys. Chem. C. **113**, 20896 (2009)
32. H. Xie, N. Hu, L. Wang, Y. Lin, R. Xiong, Z. Yu, W. Tang, Q. Wang, J. Shi, Doping effect on electronic transport properties of $Sr_{14}(Cu_{1-y}M_y)_{24}O_{41}$ (M = Zn, Ni). Phys. B **381**, 168–173 (2006)
33. T. Osafune, N. Motoyama, H. Eisaki, S. Uchida, Optical study of the $Sr_{14-x}Ca_xCu_{24}O_{41}$ system: evidence for hole-doped Cu_2O_3 ladders. Phys. Rev. Lett. **78**, 1980–1983 (1997)